Thermal conductivity of commodity polymers under high pressures

Otavio Higino Moura de Alencar,[1,2] James Wu,[3,4] Marcus Müller,[5] and Debashish Mukherji[3,5,*]

[1] *CentraleSupélec, Université Paris–Saclay, 91190 Gif–sur–Yvette, France*
[2] *Centro de Tecnologia, Universidade Federal do Ceará, 60455-760 Fortaleza, Ceará, Brazil*
[3] *Quantum Matter Institute, University of British Columbia, Vancouver BC V6T 1Z4, Canada*
[4] *Department of Physics, University of California, Berkeley, California 94720, United States*
[5] *Institut für Theoretische Physik, George–August–Universität Göttingen, 37077 Göttingen, Germany*

Understanding the thermal conductivity of polymers under high–pressure conditions is essential for a range of applications, from aerospace and deep–sea engineering to common lubricants. However, the complex relationship between pressure, P, the thermal transport coefficient, κ, and polymer architecture poses substantial challenges to both experimental and theoretical investigations. In this work, we study the pressure–dependent thermal transport properties of a widely used commodity polymer – poly(methyl methacrylate) (PMMA) – using a combination of all–atom molecular dynamics simulations and semi-analytical approaches. While we report both classical and quantum-corrected estimates of κ, the latter approach reveals that as the pressure increases from 1 atm to 10 GPa, κ rises by up to a factor of four – from 0.21 W m^{-1} K^{-1} to 0.80 W m^{-1} K^{-1}. To better understand the mechanisms behind this increase, we disentangle the contributions from bonded and nonbonded monomer interactions. Our analysis shows that nonbonded energy-transfer rates increase by a factor of six over the pressure range, while bonded interactions show a more modest increase – about a factor of three. This observation further consolidates the fact that the nonbonded interactions play the dominant role in dictating the microscopic heat flow in polymers. These individual energy-transfer rates are also incorporated into a simplified heat diffusion model to predict κ. The results obtained from different approaches show internal consistency and align well with available experimental data. Additionally, some data for polylactic acid (PLA) are presented.

I. INTRODUCTION

Polymers are ubiquitous in our every life due to their lightweight nature, mechanical flexibility, chemical tunability, and cost-effectiveness [1]. Due to their spatially extended, fractal configurations [2, 3], their applications span a wide range of technologies, including aerospace components [4], deep-sea materials [5], and automotive lubricants [6, 7]. In many of these settings, polymers are subjected to demanding environmental conditions, particularly elevated pressures and temperatures, which impose stringent requirements on thermal stability and heat dissipation. However, the intrinsically low thermal conductivity of polymers – quantified by the thermal transport coefficient κ – remains a key limitation in such applications, often restricting their performance in heat-sensitive or high-power environments.

Heat transport in polymers arises from a complex interplay between bonded interactions along the polymer backbone (e.g., carbon-carbon (C-C) bonds), nonbonded interactions (e.g., van der Waals forces or hydrogen bonds), and the overall polymer conformation [8–10]. In neutral amorphous polymers, where local (monomer level) vibrations dominated by nonbonded interactions carry heat, κ typically ranges from 0.1 to 0.4 Wm^{-1}K^{-1} [10, 11]. In contrast, when bonded interactions become dominant – such as in highly aligned or stretched polymer fibers – κ can increase significantly, reaching values between 50–100 Wm^{-1}K^{-1} for polyethylene fibers [12, 13] and 14 Wm^{-1}K^{-1} for cellulose fibers [14].

While thermal conductivity of polymers has been studied extensively under ambient conditions [8–10], relatively little is known about their behavior at elevated pressures [15–19]. High pressure is expected to exert a pronounced influence on heat flow, as chains can densify, reorganize, or undergo phase transitions – all of which can markedly influence κ. The nontrivial coupling between pressure-induced structural changes and the different modes of energy transfer in polymers make this a challenging yet important area of study.

In this work, we employ all-atom molecular dynamics simulations to investigate the pressure dependence of thermal conductivity in two representative commodity polymers: poly(methyl methacrylate) (PMMA) and polylactic acid (PLA). The macroscopic κ is computed using a standard nonequilibrium approach-to-equilibrium method [20], and the quantum-corrected values are estimated using an approach that properly accounts for the vibrational modes contributing to κ at a given temperature and pressure [21]. To gain microscopic insight, we utilize a single-chain energy-transfer model [22, 23] to examine how pressure modulates energy transfer between monomers, both bonded and nonbonded, and how these microscopic changes affect the macroscopic κ. By decoupling these contributions and embedding them within a simplified diffusion model, we aim to uncover the underlying mechanisms that govern thermal transport in polymers under extreme pressures. This understanding may offer valuable insights for

* debashish.mukherji@theorie.physik.uni-goettingen.de

designing materials optimized for high-pressure applications.

The remainder of this manuscript is organized as follows: Section II introduces the computational method, including the relevant material-specific details. Section III presents the results. Finally, conclusions are drawn in Section IV.

II. MATERIALS, MODELS AND METHODS

A. Polymer models

As test cases, we simulate two widely used commodity polymers: poly(methyl methacrylate) (PMMA) and polylactic acid (PLA). While both polymers are of interest, our analysis will primarily focus on PMMA due to the extensive availability of experimental data for comparison. PMMA is modeled using a modified version of the OPLS-AA force field, as described in Ref. [24], while PLA is represented using the standard OPLS-AA parameters [25]. These force field choices have been previously validated, accurately capturing the conformational behavior of single PMMA chains in solution [24], as well as reproducing the heat capacities of PMMA [26] and PLA [21], and the thermal conductivity of both polymers [21].

Each system consists of $N_c = 100$ polymer chains, with each chain composed of $N_\ell = 30$ monomer units. In this work, we utilize previously equilibrated, solvent-free PMMA [26] and PLA [21] configurations. All systems were initially equilibrated in their melt state at a temperature $T = 600$ K under ambient pressure (1 atm), and subsequently quenched down to $T = 300$ K. Further methodological details are presented in the corresponding sections.

B. Simulation details

All simulations are performed using the GROMACS molecular dynamics package [27]. While the initial configurations are taken from our previous studies, in the present work we re-equilibrate the systems at each target pressure P at a fixed temperature of $T = 300$ K. Temperature is controlled using a Langevin thermostat with a time constant $\tau_{\mathrm{T}} = 1.0$ ps. Pressure P is varied from 1 atm to 10 GPa, and is maintained using the Parrinello-Rahman barostat with a time constant $\tau_{\mathrm{p}} = 0.5$ ps. These simulations are performed for 1 μs at each P, where the integration time is chosen to be $\Delta t = 1$ fs. After equilibration at each P, we compute key observables – including the thermal conductivity κ, monomer-level energy-transfer rates, and elastic constants C_{ij} – all at $T = 300$ K.

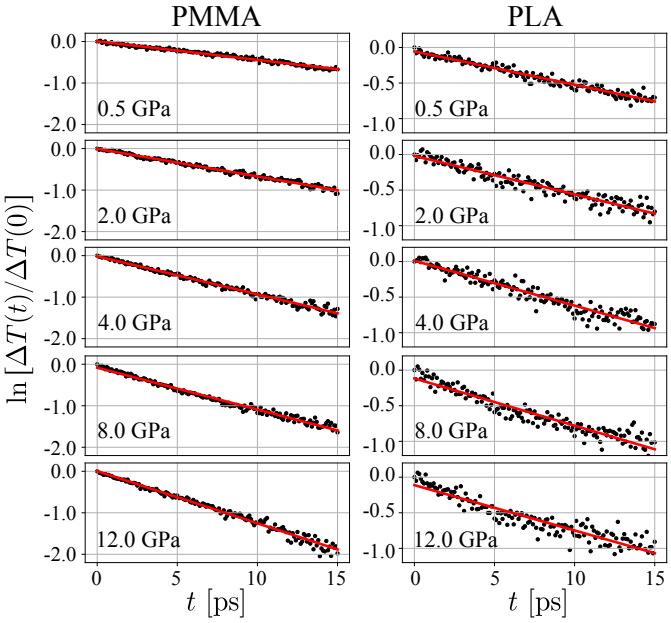

FIG. 1: Time evolution of the kinetic temperature difference between hot and cold slabs, $\Delta T(t) = T_{\mathrm{hot}}(t) - T_{\mathrm{cold}}(t)$, for (left) poly(methyl methacrylate) (PMMA) and (right) polylactic acid (PLA). Results are shown for different pressures P. Solid lines represent exponential fits, from which the thermal conductivity κ is extracted using Equation 1. Note that slightly larger fluctuations in the PLA data is because it consists of a smaller number of atoms within the simulation domain owing to its smaller monomer size.

III. RESULTS AND DISCUSSIONS

We begin by computing the classical estimates of the thermal conductivity coefficient κ as a function of applied pressure P. For this purpose, we employ the nonequilibrium approach-to-equilibrium method [20], which we have previously validated across a range of polymeric systems [21, 23]. In this method, the simulation box is divided into two equal regions: one initialized at a higher temperature ($T_{\mathrm{hot}} = 350$ K), and the other at a lower temperature ($T_{\mathrm{cold}} = 250$ K). These temperatures are imposed using a Langevin thermostat applied for 5 ns with a timestep of $\Delta t = 1$ fs. After this initial thermalization, the thermostat is removed, and the temperature difference $\Delta T(t) = T_{\mathrm{hot}}(t) - T_{\mathrm{cold}}(t)$ is allowed to relax in the microcanonical (NVE) ensemble. The NVE simulations are carried out for 15 ps with a reduced timestep of $\Delta t = 0.1$ fs to ensure numerical stability. During this relaxation period, $\Delta T(t)$ decays naturally as heat flows from the hotter to the colder region. Figure 1 shows the transient decay of $\Delta T(t)$ for both polymers across increasing applied pressures P (from top to bottom). The decay is well described by an exponential function, $\Delta T(t) \propto \exp(-t/\tau)$, where τ is the characteristic relaxation time extracted from the fits (shown as red lines).

The relaxation times τ extracted from the temperature decay curves in Figure 1 can be used to compute κ via

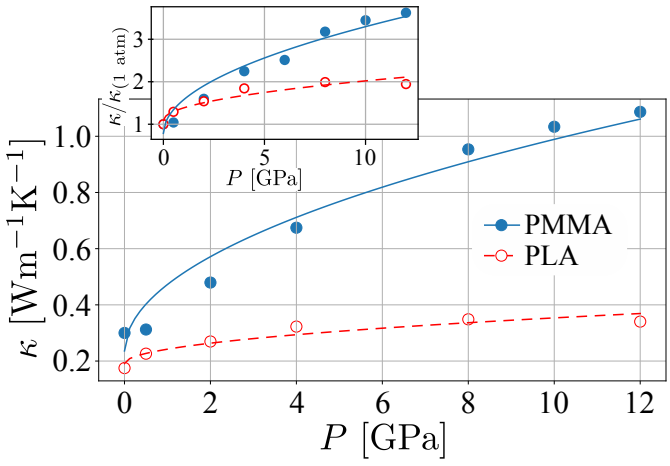

FIG. 2: The main panel shown the classical estimate of the thermal transport coefficient κ as a function of pressure P for two polymers: poly(methyl methacrylate) (PMMA) and polylactic acid (PLA), at $T = 300$ K. The lines represent fits to the empirical relation $\kappa = \kappa_1 + \kappa_2\sqrt{P}$. The inset shows the same data as the main panel but with κ normalized by its value at $P = 1$ atm, i.e., $\kappa/\kappa_{(1\ \text{atm})}$, for the respective PMMA and PLA simulations.

the following relation,

$$\kappa = \frac{1}{4\pi^2}\frac{cL}{\mathcal{A}\tau}, \tag{1}$$

where $c = 3Nk_B$ is the Dulong-Petit classical estimate of specific heat, L is the length of the simulation domain along the direction of heat flow, and $\mathcal{A}$ is the cross-sectional area perpendicular to that direction. Here, N is the total number of atoms in the systems and k_B is the Boltzmann constant.

As expected, the relaxation of $\Delta T(t)$ accelerates progressively with increasing P, indicating enhanced heat transfer under compression. This trend is reflected in the pressure-dependent increase of κ, as shown in the main panel of Figure 2, and is consistent with previous observations of pressure-enhanced thermal transport in polymers [15–19]. Quantitatively, as pressure increases from 1 atm to approximately 12 GPa, κ increases by a factor of about 2.0 for PLA and around 3.5 for PMMA (see the inset in Figure 2). The observed increase in κ can be interpreted within the framework of the minimum thermal conductivity model [19, 28], which connects κ to both the material's stiffness and atomic number density ρ_N. Under increasing P, the stiffness (i.e., the elastic moduli) tends to grow approximately linearly with P, while ρ_N remains relatively unchanged. This results in an empirical scaling of the form $\kappa = \kappa_1 + \kappa_2\sqrt{P}$, which has been previously validated in experimental studies [19] and is used here to fit our simulation data of classical κ using Equation 1. Our simulation results are well described by this empirical model, as evidenced by the fitted curves in Figure 2. The best fit parameters obtained from the simulations are $\kappa_1 = 0.191$ $\text{Wm}^{-1}\text{K}^{-1}$ and $\kappa_2 = 0.051$ $\text{Wm}^{-1}\text{K}^{-1}\text{GPa}^{-1/2}$ for PLA, and $\kappa_1 = 0.239$ $\text{Wm}^{-1}\text{K}^{-1}$ and $\kappa_2 = 0.234$ $\text{Wm}^{-1}\text{K}^{-1}\text{GPa}^{-1/2}$ for PMMA. At a later stage in this work, we will come back to the effect of P on stiffness of PMMA in a more detail.

We note in passing that the absolute values of κ obtained from experiments [17, 19] are typically smaller than those estimated from our classical simulations in Figure 2. A key contribution to this discrepancy is the overestimation of the specific heat capacity c in classical models. Classical simulations assume that all vibrational modes contribute equally to c, whereas in reality, many high-frequency modes in polymers – such as C-H bond vibrations with characteristic frequencies around $\nu = 90$ THz – remain quantum mechanically frozen at room temperature ($T = 300$ K, corresponding to approximately $\nu = 6.2$ THz) [26]. When κ is corrected by incorporating the appropriate contributions from the vibrational density of states at a given temperature, the simulation results show good agreement with experimental measurements [21].

The discussions in the preceding paragraphs invoke a few fundamental questions:
(i) What is the role of the increased atomic number density ρ_N with pressure P in governing monomer-level energy-transfer rates?
(ii) How does the monomer-level energy transfer influences macroscopic κ?
(iii) How does the interplay between ρ_N and the inherent increase in material stiffness with P influence the thermal conductivity κ?
(iv) Can quantum-corrected κ data offer deeper insight into the underlying physical mechanisms?
To address these questions, we employ three recently proposed techniques: (1) the single-chain energy-transfer model [22, 23], (2) a noise-canceling method for accurately estimating the components of the elastic modulus tensor C_{ij} [29, 30], and (3) a framework for calculating quantum-corrected κ using the exact vibrational density of states $g(\nu)$ [21], under the assumptions of the minimum thermal conductivity model [28].
In the following sections, we apply these approaches to gain deeper insight into thermal transport under high-pressure conditions. Given the availability of detailed experimental data for PMMA, our analysis will primarily focus on this system.

A. Effect of pressure on monomer-level energy transfers

Macroscopic κ in polymers is typically low. However, at the microscopic (monomer) level, energy transfer occurs through distinct pathways: (i) between two bonded monomers, and (ii) between a monomer and its n non-bonded nearest neighbors. For instance, a typical bonded interaction in polymers is the C-C covalent bond, which has a bond strength of approximately $80k_BT$ at $T = 300$ K and a stiffness exceeding 250 GPa [31]. In contrast,

nonbonded interactions in neutral polymers are primarily governed by van der Waals and hydrogen bonds, with interaction strengths ranging from 1 to 4 $k_{\mathrm{B}}T$ [32, 33]. As a result of these much stiffer bonded interactions, heat transfer between covalently bonded monomers is significantly faster than between nonbonded monomers. A model capable of decoupling these two distinct microscopic energy-transfer rates along these pathways is the single-chain energy-transfer model (SCETM) [22, 23].

SCETM is based on a simplified yet effective picture in which an energy packet primarily diffuses along the polymer backbone via stiff bonded interactions through successive hops. Occasionally, the energy also transfers off the chain to nearest-neighbor nonbonded monomers. Within this framework, the time evolution of the internal energy $\mathcal{E}_i = c_{\mathrm{mon}} T_i$ of the i^{th} monomer can be expressed as,

$$\begin{aligned}\frac{\mathrm{d}T_i}{\mathrm{d}t} &= \frac{G_{\mathrm{b}}}{c_{\mathrm{mon}}}(T_{i+1} - 2T_i + T_{i-1}) \\ &+ \frac{\tilde{G}_{\mathrm{b}}}{c_{\mathrm{mon}}}(T_{i+2} - 4T_{i+1} + 6T_i - 4T_{i-1} + T_{i-2}) \\ &+ \frac{nG_{\mathrm{nb}}}{c_{\mathrm{mon}}}(T_{\mathrm{bulk}} - T_i)\,,\end{aligned} \tag{2}$$

where $G_{\mathrm{b}}/c_{\mathrm{mon}}$ and $\tilde{G}_{\mathrm{b}}/c_{\mathrm{mon}}$ denote the energy-transfer rates via bonded and next-nearest bonded interactions along the chain, respectively, while $G_{\mathrm{nb}}/c_{\mathrm{mon}}$ accounts for the nonbonded energy-transfer rate. Here, c_{mon} is the specific heat of a single monomer, and the bulk temperature is taken to be $T_{\mathrm{bulk}} = 300$ K. It is important to note that Equation 2 explicitly includes only first and second nearest-neighbor bonded interactions along the chain backbone, which are typically the dominant contributors to intrachain energy transport.

Following Ref. [22, 23], diagonalizing Equation 2 along the polymer chain contour yields a set of exponentially relaxing temperatures of eigenmodes,

$$\hat{T}_p\,(t) \propto e^{-\alpha_p t}, \tag{3}$$

where $\hat{T}_p(t)$ represents the p^{th} mode of the cosine-transformed temperature, defined as

$$\hat{T}_p(t) = \sum_{i=0}^{N_\ell - 1} [T_i(t) - T_{\mathrm{bulk}}] \cos\left[\frac{p\pi}{N_\ell}\left(i + \frac{1}{2}\right)\right], \tag{4}$$

and the corresponding relaxation rate α_p is given by,

$$\alpha_p = 4\frac{G_{\mathrm{b}}}{c_{\mathrm{mon}}}\sin^2\left(\frac{p\pi}{2N_\ell}\right) - 16\frac{\tilde{G}_{\mathrm{b}}}{c_{\mathrm{mon}}}\sin^4\left(\frac{p\pi}{2N_\ell}\right) + n\frac{G_{\mathrm{nb}}}{c_{\mathrm{mon}}}. \tag{5}$$

To calculate the relaxation rates α_p, we have used the exact same protocol as in our earlier works [23, 34]. For this purpose, we performed a separate set of targeted simulations using a localized thermal perturbation protocol. Specifically, the 16^{th} monomer of a single PMMA chain was initialized at an elevated temperature of $T_{16\mathrm{th}} = 1000$ K, while all other monomers in the system were maintained at the reference bulk temperature $T_{\mathrm{bulk}} = 300$ K. This initial thermal configuration was generated through canonical simulations. Following this thermalization phase, the elevated temperature $T_{16\mathrm{th}}$ was allowed to relax naturally during microcanonical simulations, thereby enabling energy transfer from the hot monomer to its bonded neighbors along the chain and to nonbonded neighbors from surrounding chains. To ensure statistically reliable results, this procedure was repeated for 600 independent realizations by randomly selecting different PMMA chains from the homogeneous bulk and initializing velocities using different random seeds. The canonical thermalization are performed for 1 ns with $\Delta t = 1$ fs, followed by 20 ps of microcanonical relaxation with $\Delta t = 0.1$ fs. The short NVE simulations were sufficient to capture the early-time dynamics of energy redistribution from the initially hot monomer.

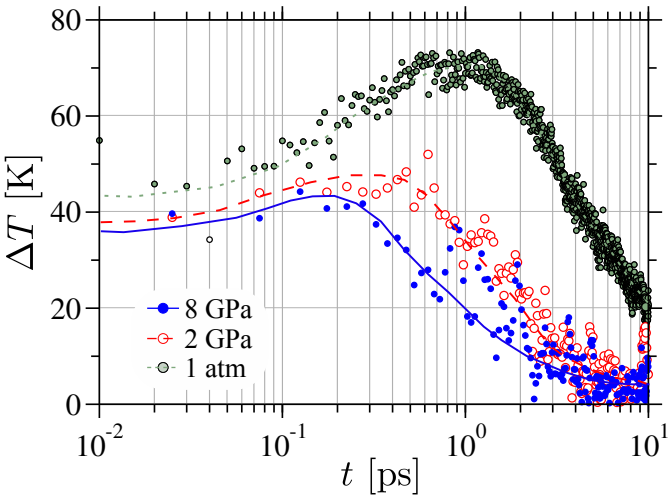

FIG. 3: Temperature profiles ΔT as a function of time during the relaxation of a central monomer initially heated to 1000 K. The data correspond to its first nearest bonded neighbors, shown for three different pressures P. Lines are included as visual guides. The data for 1 atm is taken from Ref. [23].

In Figure 3, we show the temperature evolution of the first bonded neighbor of a hot monomer during NVE simulations. As expected, the temperature of this neighbor initially rises as it receives energy from the hot monomer, and subsequently decays back to the reference temperature of $T = 300$ K (i.e., $\Delta T = 0$ K). This relaxation occurs as the heat is redistributed along the bonded backbone and toward surrounding nonbonded neighbors. Two features are visible with increasing P: (i) the peak shifts towards shorter time and (ii) peak height decreases. This former trend reflects a faster and more efficient redistribution of energy between monomers under compression and can be directly linked to the relaxation rates α_p of the underlying temperature modes. Moreover, it also helps explain the latter observation (ii), which is addressed in the following analysis.

TABLE I: A table summarizes the energy-transfer rates between different types of monomer pairs, specifically: nearest neighbor nonbonded monomers $G_{\rm nb}/c_{\rm mon}$, bonded monomers $G_{\rm b}/c_{\rm mon}$, and next-nearest bonded monomers $\tilde{G}_{\rm b}/c_{\rm mon}$. Additionally, we list the thermal transport coefficients obtained directly from simulations κ alongside the theoretical predictions based on the SCETM model $\kappa_{\rm theory}$ using Equation 6. The data are presented for poly(methyl methacrylate) (PMMA) for three different pressure P at the reference temperature $T = 300$ K.

P	$G_{\rm nb}/c_{\rm mon}$ [ps^{-1}]	$G_{\rm b}/c_{\rm mon}$ [ps^{-1}]	$\tilde{G}_{\rm b}/c_{\rm mon}$ [ps^{-1}]	$G_{\rm b}/G_{\rm nb}$	κ [Wm^{-1}K^{-1}]	$\kappa_{\rm theory}$ [Wm^{-1}K^{-1}]
1 atm	0.024	1.49	0.72	61.07	0.31	0.16
2 GPa	0.119	3.12	1.59	26.10	0.48	0.44
8 GPa	0.152	4.22	1.99	27.72	0.95	0.62

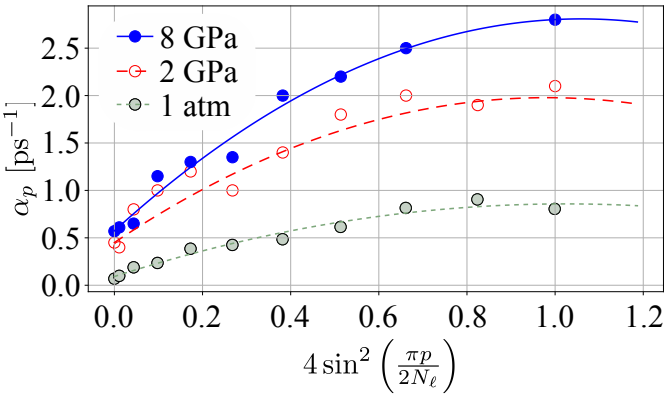

FIG. 4: The relaxation rates α_p of the cosine-transformed temperature modes $\hat{T}_p(t)$ are plotted as a function of $4\sin^2(\pi p/2N_\ell)$. The data correspond to poly(methyl methacrylate) (PMMA) at a temperature of $T = 300$ K, with representative results shown for three different applied pressures P. The dataset for ambient pressure (1 atm) is taken from Ref. [23]. The solid lines represent fits to the data using Equation 5.

In Figure 4, we present the relaxation rates α_p as a function of the mode index p, which are well captured by the theoretical prediction provided in Equation 5. The corresponding energy-transfer rates – specifically for bonded $G_{\rm b}$, next-nearest bonded $\tilde{G}_{\rm b}$, and nonbonded $G_{\rm nb}$ – are extracted from fits to the data and summarized in Table I. A clear and systematic pressure dependence is observed, particularly in the nonbonded energy-transfer channel, which are dominated by relatively soft interactions. As pressure is increased from 1 atm to 8 GPa, the nonbonded energy transfer rate $G_{\rm nb}$ increases significantly, by approximately a factor of 5–6. In contrast, the energy-transfer rate $G_{\rm b}$ between bonded monomers increases more modestly, by a factor of roughly 2–3 over the same pressure range. This disparity reflects the different sensitivities of bonded and nonbonded interactions to external pressure. Compression leads to a pronounced increase in local packing density, which enhances the frequency and strength of intermolecular (nonbonded) contacts. As a result, $G_{\rm nb}$ becomes substantially larger at higher pressures, which leads a substantial amount of energy leakage via the nonbonded contacts and is the main reason why the peak intensities of ΔT in Figure 3 decrease with P. On the other hand, bonded interactions – determined by the intrinsic stiffness of covalent bonds – are relatively less effected by compression of up to 10 GPa, leading to a smaller variation in $G_{\rm b}$.

When we refer to bonded energy transfer, we are referring to the transfers involving all atoms within a monomer to its neighboring bonded monomer. The effective bond lengths between the center-of-masses of two successive monomer are influenced by compression and local packing. In contrast, the lengths of bare covalent bonds – such as C-C bonds (i.e., around 0.15 nm) – remain essentially unchanged even at pressures up to 10 GPa.

Collectively, the increase in microscopic energy-transfer rates under elevated pressure leads to the observed enhancement in the macroscopic thermal conductivity κ. To quantify this behavior, we utilize a simplified theoretical estimate of κ previously proposed in Ref. [23], which incorporates contributions from distinct energy-transfer pathways,

$$\kappa_{\rm theory} = \frac{\rho}{6}\left[nG_{\rm nb}r_{\rm nb}^2 + \left(G_{\rm b} - 4\tilde{G}_{\rm b}\right)r_{\rm b}^2 + \tilde{G}_{\rm b}\tilde{r}_{\rm b}^2\right], \quad (6)$$

Here, ρ is the monomer number density, and $r_{\rm nb}$, $r_{\rm b}$, and $\tilde{r}_{\rm b}$ represent the characteristic interaction distances for nonbonded, bonded, and next-nearest bonded monomers, respectively. This expression effectively combines the contributions from each energy-transfer mechanism into a single estimate for thermal conductivity. The calculated values of $\kappa_{\rm theory}$ are summarized in the last column of Table I. The pressure-dependent increase in κ – typically by a factor of 3 to 4 – is consistent across all methods used, underscoring the robustness of the SCETM-based approach and the simplified diffusion-like model in capturing the essential physics of thermal transport under compression. It is worth noting, however, that the absolute values of $\kappa_{\rm theory}$ tend to underestimate those obtained from classical nonequilibrium simulations, see the second last column Table I. This discrepancy has also been reported in previous studies [23, 34] across a range of polymers and likely reflects the idealizations inherent in the simplified theoretical framework as well as quantum corrections discussed below.

We are currently unable to pinpoint the precise origin of the discrepancy between κ_{theory} and simulation-based estimates, which typically ranges between a factor of 1/4 to 2/3 across the various systems studied here as well as in Refs. [23, 34]. Nor can we fully explain how this deviation is influenced by factors such as polymer stiffness, monomer chemistry, or monomer size. However, it is worth noting that the simplistic model used to estimate κ_{theory} is based primarily on nearest-neighbor nonbonded energy transfer, while neglecting cascading or multi-step heat transfer events across extended nonbonded networks. This simplification may be significant, as thermal transport in amorphous polymers is often dominated by complex, collective interactions involving many-body nonbonded contacts. A more comprehensive treatment that accounts for these longer-range or higher-order energy-transfer pathways is likely needed to improve the quantitative accuracy of κ_{theory}. A detailed investigation of these mechanisms lies beyond the scope of the present work and will be addressed in future studies.

We note in passing that the analysis in Figure 4 includes modes up to $p = 11$, which corresponds to a spatial resolution of roughly three monomers – approximately equal to the persistence length of a PMMA chain. Below this length scale, energy transport is expected to be ballistic rather than diffusive. Consequently, the assumptions underlying the SCETM, which is based on diffusive transport, may no longer be valid in this regime.

B. Quantum estimate of κ

So far, we have discussed the microscopic energy-transfer rates and the influence of pressure P on monomer-level thermal properties within a classical framework. However, it is important to recognize that in experimental systems of amorphous polymers, the macroscopic κ is largely governed by low-frequency, vibrational modes – primarily associated with soft, nonbonded interactions. In contrast, the high-frequency modes corresponding to stiff covalent bonds (such as C-H or C-C stretching modes) remain quantum-mechanically inactive – or frozen – at ambient conditions due to their large energy quanta relative to $k_{\text{B}}T$ [26]. Classical simulations, however, treat all vibrational modes as fully accessible at all temperatures. This results in a systematic overestimation of κ in comparison to experimental measurements [7, 21], even when highly accurate force fields are employed and simulations are conducted with meticulous care. This fundamental limitation of classical models motivates the need for quantum corrections.

To address this discrepancy, a quantum-corrected approach has been developed based on the original minimum thermal conductivity model [28], augmented with the exact vibrational density of states $g(\nu)$, obtained from simulation [21]. This method has proven effective in describing thermal transport in a wide range of amorphous polymer systems [21], including cellulose derivatives [35]. Within this framework, the thermal conductivity $\kappa(T, P)$ is expressed as

$$\kappa(T,P) = \left(\frac{\rho_{\text{N}} h^2}{6 k_{\text{B}} T^2}\right)\left(v_\ell^2 + 2v_t^2\right)\int \frac{\nu e^{h\nu/k_{\text{B}}T}}{\left(e^{h\nu/k_{\text{B}}T}-1\right)^2} g(\nu)\mathrm{d}\nu, \tag{7}$$

where ρ_{N} is the atomic number density, and v_ℓ and v_t are the longitudinal and transverse sound velocities, respectively. These velocities are determined from the elastic moduli and mass density ρ_{m} via $v_\ell = \sqrt{C_{11}/\rho_{\text{m}}}$ and $v_t = \sqrt{C_{44}/\rho_{\text{m}}}$. Equation 7 requires accurate estimates of ρ_N, $g(\nu)$, and the components of v_{i}. We will now individually compute these quantities and use them to obtain an estimate of the quantum-corrected κ.

Vibrational density of states: To compute $g(\nu)$ at different pressures, we use the Fourier transform of the normalized mass-weighted velocity autocorrelation function $\psi(t)$ using, $g(\nu) = \frac{1}{A}\int_0^\infty \cos(2\pi\nu t)\frac{\psi(t)}{\psi(0)}\mathrm{d}t$ [36], where the normalization constant A ensures $\int_0^\infty g(\nu), \mathrm{d}\nu = 1$. The function $\psi(t)$ is given by, $\psi(t) = \sum_i m_i \langle \vec{v}_i(t)\cdot\vec{v}_i(0)\rangle$, and represents the superposition of contributions from all vibrational modes in the system. For the computation of $\psi(t)$, we use a timestep of $\Delta t = 0.1$ fs and sample data over a 10 ps interval, with an output frequency of 5×10^{-4} ps. This ensures accurate resolution of both low- and high-frequency vibrational contributions.

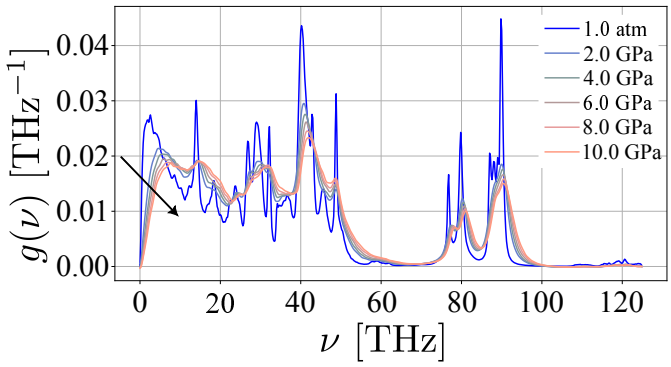

FIG. 5: The vibrational density of states $g(\nu)$ for poly(methyl methacrylate) (PMMA) at various pressures P, measured at a temperature of $T = 300$ K. The arrow indicates the direction of increasing P.

In Figure 5, we present representative $g(\nu)$ for PMMA at different P. A prominent feature emerging from $g(\nu)$ is the progressive smoothing of the spectral profile with increasing P. At ambient conditions, $g(\nu)$ typically exhibits pronounced peaks and irregularities that are a direct consequence of the amorphous, disordered nature of polymeric systems. These spectral features arise due to a wide distribution of local environments and bonding configurations, particularly in the nonbonded interactions that dominate the low-frequency regime. However, as pressure is increased, the local packing density of monomers becomes more homogeneous, and the sys-

tem undergoes a form of pressure-induced structural ordering at the microscopic scale. This densification under compression reduces the magnitude of thermal fluctuations and local configurational heterogeneity, thereby suppressing the vibrational spectrum. Consequently, the sharp peaks and valleys in $g(\nu)$ gradually flatten out, and the distribution of vibrational modes becomes more uniform. Additionally, the peaks in $g(\nu)$ shift towards higher frequencies with increasing P, which is indicative of an overall stiffening of the vibrational modes. This is consistent with the enhanced stiffness of PMMA under pressure [19], particularly in the nonbonded interactions where increased packing leads to steeper effective potentials between neighboring monomers.

The smoothing of $g(\nu)$ has further implications for thermal transport. A more uniform vibrational spectrum with stiffer modes contributes to a higher thermal conductivity, as energy can be transferred more efficiently through vibrational excitations that are less scattered by structural disorder. This observation supports the broader conclusion that compression enhances thermal transport in polymers not only through mechanical stiffening, but also by reducing vibrational scattering mechanisms inherent to amorphous systems.

Sound-wave velocities: To determine the sound-wave velocities v_ℓ and v_t, the elastic constants C_{11} and C_{44} are first computed at finite temperature using a recently proposed method [30]. This method is specifically designed to overcome the limitations posed by thermal noise in molecular dynamics simulations. This approach builds on a noise-cancellation strategy originally introduced for the calculation of piezoelectric coefficients in crystalline silica [29], and has since been adapted to provide precise estimates of elastic moduli in amorphous commodity polymers [30] and cellulose derivatives [35]. The key idea is to apply symmetric strain fields and extract stress differences, thereby averaging out stochastic thermal fluctuations that typically obscure the small stress responses associated with elastic deformations.

The shear modulus C_{44} is computed by imposing a volume-conserving, anisotropic deformation to an initially cubic simulation cell of side length L. The deformation is applied such that, $L_x = L(1+\varepsilon)$, $L_y = L/(1+\varepsilon)$, and $L_z = L$, ensuring the total volume remains constant to isolate the shear response. A small strain $\varepsilon = 10^{-3}$ is used to remain within the linear elastic regime. Under these conditions, C_{44} can be computed from the change in stress components using either of the following equivalent expressions;

$$C_{44} = \frac{\sigma_{xx}(+\varepsilon) - \sigma_{xx}(0)}{2\varepsilon} \quad \text{or} \quad C_{44} = -\frac{\sigma_{yy}(-\varepsilon) - \sigma_{yy}(0)}{2\varepsilon}, \tag{8}$$

where σ_{ij} refers to the stress tensor component measured in the deformed configurations.

The longitudinal modulus C_{11} is extracted by applying uniaxial strains in the x-direction in two separate simulations using, $L_x = L(1\pm\varepsilon)$, while keeping the box lengths along y and z fixed. The corresponding difference in the

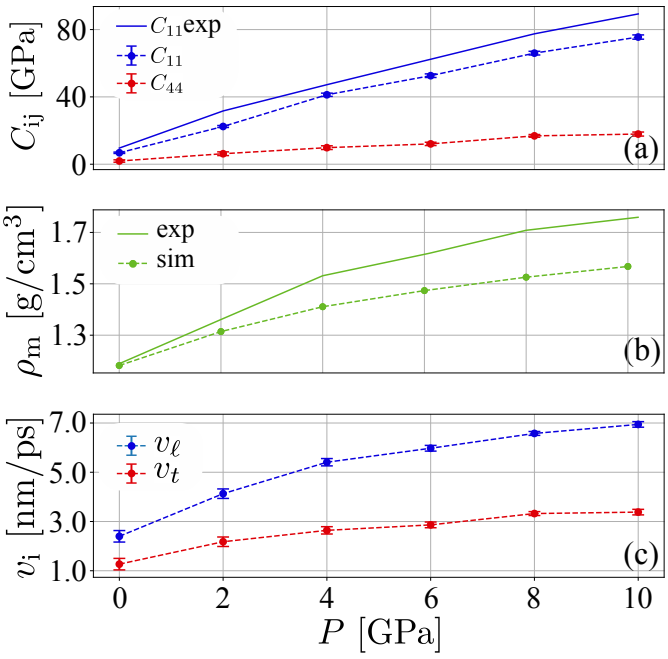

FIG. 6: Pressure dependence of the components of the elastic modulus tensor C_{ij} (part a), mass density ρ_m (part b), and components of the sound-wave velocities v_i (part c). The data is shown for a poly(methyl methacrylate) sample and at a temperature of $T = 300$ K. For comparison, we have also included the available C_{11} experimental data of PMMA [19] in part a. Experimental data for ρ_m is also included in part b [37].

axial stress response yields;

$$C_{11} = \frac{\sigma_{xx}(+\varepsilon) - \sigma_{xx}(-\varepsilon)}{2\varepsilon}. \tag{9}$$

This symmetric strain protocol ensures that any nonlinear or temperature-induced offsets are eliminated, enabling accurate determination of elastic constants even in thermally active systems. Overall, this methodology offers a robust means of evaluating elastic properties from finite-temperature simulations, particularly useful for disordered systems like polymers where standard stress-strain methods often suffer from poor signal-to-noise ratios.

In Figure 6(a), we show the pressure dependence of the elastic constants C_{11} and C_{44}, as well as the associated longitudinal v_ℓ and transverse v_t sound velocities in Figure 6(c). These quantities are key inputs for understanding how mechanical stiffness changes with pressure, and they also directly influence thermal transport in polymeric systems [11, 19]. As pressure increases from 1 atm to 10 GPa, both C_{11} and C_{44} increase by nearly an order-of-magnitude. This strong stiffening reflects the suppression of molecular motion and enhanced intermolecular forces as the polymer chains are packed more tightly. In contrast, the mass density ρ_m increases by a comparatively moderate 25% across the same pressure range. This indicates that while compression does densify the

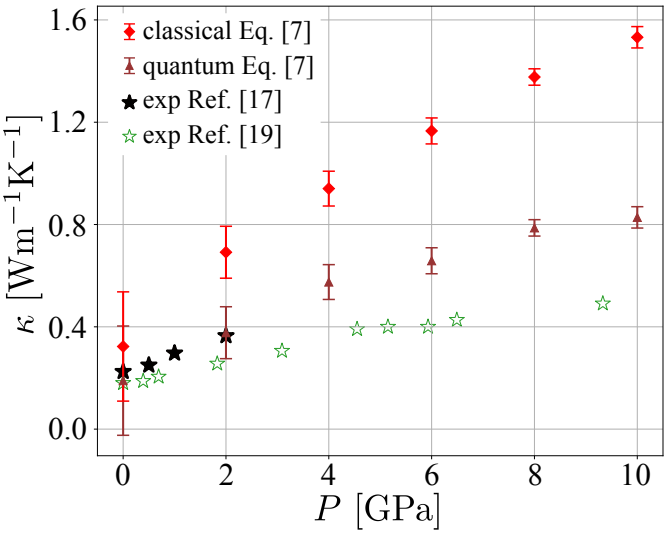

FIG. 7: Thermal transport coefficient κ as a function of pressure P for poly(methyl methacrylate) (PMMA) at a fixed temperature of $T = 300$ K. The data presented correspond to κ values obtained using multiple computational approaches. Classical estimates are calculated using Equation 7 in the high-temperature limit, where all vibrational modes are thermally active (solid diamonds). Quantum-corrected estimates of the thermal conductivity κ are calculated using the full expression given in Equation 7 (solid triangles). For comparison, experimental measurements from Ref. [17] are included for pressures up to 2 GPa (solid stars), while additional data spanning the full pressure range (open stars) are taken from Ref. [19].

system, the relative change in density is much smaller than the increase in stiffness. It can also be appreciated that C_{ij} increases almost linearly, especially for the higher pressures.

Using the above computed vibrational density of states $g(\nu)$ and pressure-dependent sound velocities v_{i}, we calculated the quantum-corrected thermal transport coefficient κ at various pressures using Equation 7. These results are presented in Figure 7. As expected, incorporating quantum corrections significantly improves agreement with experimental data. In the low-pressure regime ($P \leq 2.0$ GPa), the quantum-corrected κ shows notably good agreement with the experimental results in Ref. [17], indicated by solid stars in Figure 7. This consistency serves as an important validation of the modeling approach, including the methodology used for calculating $g(\nu)$ and the elastic constants, from which the sound velocities v_{i} are derived. However, at higher pressure, a growing deviation appears between the simulation-based quantum-corrected κ and the experimental data reported in Ref. [19], shown as open stars. This difference may arise from multiple sources:
(i) One potential cause lies in the pressure dependence of the mass density ρ_{m} in Figure 6(b), which plays a central role in determining both the sound velocities and the prefactor in Equation 7. As seen in Figure 6(b), the experimentally measured ρ_{m} may be overestimated, particularly at high pressures. Since the sound velocities are inversely proportional to $\sqrt{\rho_{\mathrm{m}}}$, any overestimation in density directly leads to lower values of v_ℓ and v_t, and hence smaller predicted values of κ.
(ii) Different experimental techniques often result in variations in reported κ values, especially under high-pressure conditions where accurate control and measurement are challenging. Furthermore, the compressive effects on polymer microstructure – such as chain alignment, segmental ordering, or densification – may not be fully captured in the simulations unless large-scale rearrangements or long time scales are sampled.
(iii) The quantum correction in Equation 7 assumes an isotropic material, which may become less accurate as pressure alters the local packing and potentially induces structural anisotropies. These assumptions might be violated at high pressures where subtle short-range ordering can emerge, especially in systems like polymers.
(iv) Although the vibrational density of states is calculated from simulations and includes anharmonic effects, its precise shape under the high-pressure conditions – in particular, the high-frequency tail – can critically influence the integral in Equation 7. Small discrepancies in this region, which is harder to sample accurately due to lower thermal population, may lead to noticeable differences in the final computed κ.
(v) Another likely source of discrepancy is the force-field itself, which is typically parameterized at ambient conditions and may not accurately capture pressure-induced changes in interatomic interactions, molecular packing, or segmental dynamics. In particular, nonbonded parameters may inadequately represent repulsive interactions at reduced intermolecular distances, and the absence of many-body or polarization effects further limits the transferability of force-field to high-pressure regimes. Despite these deviations, the quantum-corrected results capture the essential physics of pressure-enhanced κ in polymers. The level of agreement with at least one set of experimental data is encouraging, especially considering the relatively simple form of the model and the inherent complexity of amorphous polymer systems. Overall, this analysis supports the view that combining simulation-based structural and vibrational data with quantum-informed models offers a powerful and predictive framework for exploring thermal transport properties under extreme thermodynamic conditions.

IV. CONCLUSIONS

In this work, we presented a comprehensive investigation into the pressure P dependence of thermal transport in amorphous polymers, focusing specifically on poly(methyl methacrylate) (PMMA) and polylactic acid (PLA). Using classical molecular dynamics simulations complemented by a theoretical framework, we systematically quantified how pressure enhances the thermal trans-

port coefficient κ in these materials.

Our simulations reveal a pronounced increase in κ with P, with PMMA exhibiting a nearly 3.5-fold enhancement and PLA a 2-fold increase as P is raised from ambient conditions to 12 GPa. According to the minimum thermal conductivity model [28], this trend can be attributed to the intrinsic stiffening of the amorphous polymer under compression. These results are consistent with and extend previous experimental findings [17, 19], offering both validation and new insight into pressure-mediated thermal behavior in amorphous polymers.

To understand the microscopic origin of this enhancement, we employed the single-chain energy-transfer model (SCETM) [22, 23], which decouples energy flow along bonded and nonbonded pathways within the polymer. Our analysis demonstrates that pressure most significantly amplifies the nonbonded energy-transfer rate G_{nb} – by nearly a factor of 6 – as local packing increases and interactions become more prominent. In contrast, the transfer rate between bonded monomers G_{b} rises more modestly, by a factor of 2–3. This distinct response highlights the importance of nonbonded interactions in dictating thermal transport in the amorphous polymers, especially under compression. Additionally, we validated a simplistic expression for estimating κ from microscopic energy-transfer rates, which shows same trends as our simulation data.

We further explored the elastic properties of these systems under pressure using a newly developed, noise-reducing technique for calculating the elastic constants C_{11} and C_{44} at finite temperatures [30]. This methodology provides accurate estimates of pressure-dependent sound velocities, which are critical for the calculation of κ.

Recognizing that classical simulations tend to overestimate κ [7, 21] – primarily because they assume full thermal activation of all vibrational modes [26] – we also incorporated quantum corrections into our analysis. By integrating the exact vibrational density of states $g(\nu)$ into the minimum thermal conductivity framework [21], we were able to account for the quantum corrections of the high-frequency vibrational modes (such as those involving stiff C-H bonds), which are inactive at room temperature. This approach yields a quantum-corrected estimate of κ that are in good agreement with experimental values and significantly improves the physical realism of our simulations.

To summarize, our study provides a multiscale, mechanistic understanding of pressure-enhanced thermal transport in polymers. We bridge atomistic insights, vibrational analysis, elastic property characterization, and macroscopic transport modeling into a coherent picture that explains how and why κ increases under compression. These findings not only deepen our fundamental understanding of heat transport in disordered polymeric materials but also offer practical guidance for designing polymer-based systems – such as thermal interface materials, flexible electronics, and insulating composites – where controlling thermal conductivity under variable mechanical conditions is crucial. Overall, this study provides microscopic insights into how pressure affects thermal transport in polymer systems and offers guiding principles for the design of polymer-based materials suited for extreme environments.

Acknowledgment: J.W. and D.M. thank the ARC Sockeye facility in British Columbia Canada within the project allocation st–mukherji–1, where the majority of these simulations were performed. We gratefully acknowledge the Gauss Centre for Supercomputing e.V. (www.gauss–centre.eu) for providing computing time through the John von Neumann Institute for Computing (NIC) on the GCS Supercomputer JUWELS at Jülich Supercomputing Centre (JSC), for additional compute time. O.H.M.A. acknowledges CAPES for supporting his stay in France within a double-degree program. Financial support for D.M. and M.M. was provided by the Bundesministerium für Technologie, Forschung und Raumfahrt (BMTRF) within the project 16ME0658K MExMeMo and European Union– NextGenerationEU. With deep appreciation, we dedicate this work to Kurt Kremer on the occasion of his 70th birthday– an inspiring colleague, cherished friend to D.M. and M.M., and a trusted mentor to D.M.

[1] P.-G. de Gennes, *Scaling Concepts in Polymer Physics*. Cornell University Press, 1979.

[2] Z.-G. Wang, "50th anniversary perspective: Polymer conformation—a pedagogical review," *Macromolecules*, vol. 50, no. 23, pp. 9073–9114, 2017.

[3] H.-P. Hsu, M. K. Singh, Y. Cang, H. Thérien-Aubin, M. Mezger, R. Berger, I. Lieberwirth, G. Fytas, and K. Kremer, "Free standing dry and stable nanoporous polymer films made through mechanical deformation," *Advanced Science*, vol. 10, no. 18, p. 2207472, 2023.

[4] W. Wright, "Polymers in aerospace applications," *Materials and Design*, vol. 12, no. 4, pp. 222–227, 1991.

[5] A. Chamley, C. Baley, M. Matabos, P. Vannier, P. M. Sarradin, F. Freyermouth, and P. Davies, "Polymer material biodegradation in the deep sea. a review," *Science of The Total Environment*, vol. 957, p. 177637, 2024.

[6] H. Gao and M. H. Müser, "Why liquids can appear to solidify during squeeze-out – even when they don't," *Journal of Colloid and Interface Science*, vol. 562, pp. 273–278, 2020.

[7] J. Ahmed, Q. J. Wang, O. Balogun, N. Ren, R. England, and F. Lockwood, "Molecular dynamics modeling of thermal conductivity of several hydrocarbon base oils," *Tribology Letters*, vol. 71, no. 2, p. 70, 2023.

[8] A. Henry, "Thermal transport in polymers," *Annual Review of Heat Transfer*, vol. 17, pp. 485–520, 2014.

[9] P. Keblinski, "Modeling of heat transport in polymers and their nanocomposites," *Handbook of Materials Modeling*, pp. 975–997, 2020.

[10] Mukherji, D., "Thermal Conductivity of Polymers: A Simple Matter Where Complexity Matters," *Macromolecular Rapid Communications*, vol. 45, p. 2400517, 2024.

[11] X. Xie, D. Li, T. Tsai, J. Liu, P. V. Braun, and D. G. Cahill, "Thermal conductivity, heat capacity, and elastic constants of water-soluble polymers and polymer blends," *Macromolecules*, vol. 49, pp. 972–978, 2016.

[12] S. Shen, A. Henry, J. Tong, R. Zheng, and G. Chen, "Polyethylene nanofibres with very high thermal conductivities," *Nature Nanotechnology*, vol. 5, no. 4, pp. 251–255, 2010.

[13] X. Wang, V. Ho, R. A. Segalman, and D. G. Cahill, "Thermal conductivity of high-modulus polymer fibers," *Macromolecules*, vol. 46, no. 12, pp. 4937–4943, 2013.

[14] G. Wang, M. Kudo, K. Daicho, S. Harish, B. Xu, C. Shao, Y. Lee, Y. Liao, N. Matsushima, T. Kodama, F. Lundell, L. D. Söderberg, T. Saito, and J. Shiomi, "Enhanced high thermal conductivity cellulose filaments via hydrodynamic focusing," *Nano Letters*, vol. 22, no. 21, pp. 8406–8412, 2022.

[15] V. P. Privalko and N. A. Rekhteta, "Thermal conductivity of polymers under elevated pressures," *High Pressure Research*, vol. 1, no. 5-6, pp. 377–381, 1989.

[16] V. P. Privalko and N. A. Rekhteta, "Effect of pressure on the thermal conductivity of polymers," *Journal of thermal analysis*, vol. 38, pp. 1083–1102, May 1992.

[17] S. P. Andersson and R. G. Ross, "Thermal conductivity and heat capacity per unit volume of poly(methyl methacrylate) under high pressure," *International Journal of Thermophysics*, vol. 15, pp. 949–962, Sep 1994.

[18] A. Dawson, M. Rides, and J. Nottay, "The effect of pressure on the thermal conductivity of polymer melts," *Polymer Testing*, vol. 25, no. 2, pp. 268–275, 2006.

[19] W.-P. Hsieh, M. D. Losego, P. V. Braun, S. Shenogin, P. Keblinski, and D. G. Cahill, "Testing the minimum thermal conductivity model for amorphous polymers using high pressure," *Phys. Rev. B*, vol. 83, p. 174205, May 2011.

[20] E. Lampin, P. L. Palla, P.-A. Francioso, and F. Cleri, "Thermal conductivity from approach-to-equilibrium molecular dynamics," *Journal of Applied Physics*, vol. 114, no. 3, p. 033525, 2013.

[21] Mukherji, D., "Computing the thermal transport coefficient of neutral amorphous polymers using exact vibrational density of states: Comparison with experiments," *Physical Review Materials*, vol. 8, p. 085601, 2024.

[22] S. Gottlieb, L. Pigard, Y. K. Ryu, M. Lorenzoni, L. Evangelio, M. Fernández-Regúlez, C. D. Rawlings, M. Spieser, F. Perez-Murano, M. Müller, and A. W. Knoll, "Thermal imaging of block copolymers with sub-10 nm resolution," *ACS Nano*, vol. 15, no. 5, pp. 9005–9016, 2021.

[23] L. Pigard, D. Mukherji, J. Rottler, and M. Müller, "Microscopic model to quantify the difference of energy-transfer rates between bonded and nonbonded monomers in polymers," *Macromolecules*, vol. 54, no. 23, pp. 10969–10983, 2021.

[24] D. Mukherji, C. M. Marques, T. Stuehn, and K. Kremer, "Depleted depletion drives polymer swelling in poor solvent mixtures," *Nature Communications*, vol. 8, p. 1374, Nov 2017.

[25] W. L. Jorgensen, D. S. Maxwell, and J. Tirado-Rives, "Development and testing of the opls all-atom force field on conformational energetics and properties of organic liquids," *Journal of the American Chemical Society*, vol. 118, pp. 11225–11236, 1996.

[26] H. Gao, T. P. W. Menzel, M. H. Müser, and D. Mukherji, "Comparing simulated specific heat of liquid polymers and oligomers to experiments," *Phys. Rev. Mater.*, vol. 5, p. 065605, 2021.

[27] M. J. Abraham, T. Murtola, R. Schulz, S. Páll, J. C. Smith, B. Hess, and E. Lindahl, "Gromacs: High performance molecular simulations through multi-level parallelism from laptops to supercomputers," *SoftwareX*, vol. 1,, pp. 19–25, 2015.

[28] D. G. Cahill, S. K. Watson, and R. O. Pohl, "Lower limit to the thermal conductivity of disordered crystals," *Physical Review B*, vol. 46, pp. 6131–6140, 1990.

[29] D. Herzbach and M. H. Müser, "Piezoelectric coefficients by molecular dynamics simulations in the constant stress ensemble: A case study of quartz," *Computer Physics Communications*, vol. 174, no. 1, pp. 17–23, 2006.

[30] D. Mukherji, M. Müller, and M. H. Müser, "Computing finite–temperature elastic constants with noise cancellation," *arXiv*, 2025.

[31] B. Crist and P. G. Hereña, "Molecular orbital studies of polyethylene deformation," *Journal of Polymer Science Part B: Polymer Physics*, vol. 34, no. 3, pp. 449–457, 1996.

[32] D. Mukherji, C. M. Marques, and K. Kremer, "Smart responsive polymers: Fundamentals and design principles," *Annual Review of Condensed Matter Physics*, vol. 11, no. Volume 11, 2020, pp. 271–299, 2020.

[33] G. R. Desiraju, "Hydrogen bridges in crystal engineering: Interactions without borders," *Accounts of Chemical Research*, vol. 35, no. 7, pp. 565–573, 2002.

[34] J. Wu and D. Mukherji, "Comparison of all atom and united atom models for thermal transport calculations of amorphous polyethylene," *Computational Materials Science*, vol. 211, p. 111539, 2022.

[35] D. Mukherji, T. E. de Oliveira, D. G. Cahill, and M. Müller, "Heat flow in solvent-free, dense amorphous and semi-crystalline cellulose derivatives," *10.26434/chemrxiv-2025-k6593*, 2025.

[36] J. Horbach, W. Kob, and K. Binder, "Specific heat of amorphous silica within the harmonic approximation," *The Journal of Physical Chemistry B*, vol. 103, pp. 4104–4108, May 1999.

[37] W. J. Carter and S. P. Marsh, *Hugoniot Equation of State of Polymers, Los Alamos National Laboratory Report*. 1995.